A disordered acidic domain in GPIHBP1 harboring a sulfated tyrosine regulates lipoprotein lipase

Kristian K. Kristensen[a,b], Søren Roi Midtgaard[c], Simon Mysling[a,b,d], Oleg Kovrov[e], Lars Bo Hansen[f], Nicholas Skar-Gislinge[c], Anne P. Beigneux[g], Birthe B. Kragelund[h], Gunilla Olivecrona[e], Stephen G. Young[g,i,1], Thomas J. D. Jørgensen[d], Loren G. Fong[g], and Michael Ploug[a,b,1]

[a]Finsen Laboratory, Rigshospitalet, DK–2200 Copenhagen N, Denmark; [b]Biotech Research and Innovation Centre, University of Copenhagen, DK–2200 Copenhagen N, Denmark; [c]Structural Biophysics, Niels Bohr Institute, University of Copenhagen, DK–2100 Copenhagen Ø, Denmark; [d]Department of Biochemistry and Molecular Biology, University of Southern Denmark, DK–5230 Odense M, Denmark; [e]Department of Medical Biosciences, Umeå University, SE-901 87 Umeå, Sweden; [f]Zealand Pharma, DK–2600 Glostrup, Denmark; [g]Department of Medicine, University of California, Los Angeles, CA 90095; [h]Department of Biology, University of Copenhagen, DK-2200 Copenhagen N, Denmark; and [i]Department of Human Genetics, University of California, Los Angeles, CA 90095

Contributed by Stephen G. Young, May 17, 2018 (sent for review April 20, 2018; reviewed by Jay D. Horton and Sampath Parthasarathy)

The intravascular processing of triglyceride-rich lipoproteins depends on lipoprotein lipase (LPL) and GPIHBP1, a membrane protein of endothelial cells that binds LPL within the subendothelial spaces and shuttles it to the capillary lumen. In the absence of GPIHBP1, LPL remains mislocalized within the subendothelial spaces, causing severe hypertriglyceridemia (chylomicronemia). The N-terminal domain of GPIHBP1, an intrinsically disordered region (IDR) rich in acidic residues, is important for stabilizing LPL's catalytic domain against spontaneous and ANGPTL4-catalyzed unfolding. Here, we define several important properties of GPIHBP1's IDR. First, a conserved tyrosine in the middle of the IDR is posttranslationally modified by O-sulfation; this modification increases both the affinity of GPIHBP1–LPL interactions and the ability of GPIHBP1 to protect LPL against ANGPTL4-catalyzed unfolding. Second, the acidic IDR of GPIHBP1 increases the probability of a GPIHBP1–LPL encounter via electrostatic steering, increasing the association rate constant (k_{on}) for LPL binding by >250-fold. Third, we show that LPL accumulates near capillary endothelial cells even in the absence of GPIHBP1. In wild-type mice, we expect that the accumulation of LPL in close proximity to capillaries would increase interactions with GPIHBP1. Fourth, we found that GPIHBP1's IDR is not a key factor in the pathogenicity of chylomicronemia in patients with the GPIHBP1 autoimmune syndrome. Finally, based on biophysical studies, we propose that the negatively charged IDR of GPIHBP1 traverses a vast space, facilitating capture of LPL by capillary endothelial cells and simultaneously contributing to GPIHBP1's ability to preserve LPL structure and activity.

hypertriglyceridemia | electrostatic steering | intrinsically disordered region | intravascular lipolysis | autoimmune disease

Lipoprotein lipase (LPL) is the central and rate-limiting enzyme for the intravascular lipolytic processing of triglyceride-rich lipoproteins (TRLs). The intravascular hydrolysis of triglycerides releases lipid nutrients for vital tissues (e.g., heart, skeletal muscle, adipose tissue) (1–3). Parenchymal cells (e.g., myocytes and adipocytes) synthesize LPL and secrete it into the interstitial spaces, but LPL's site of action is within the capillary lumen. The secreted LPL is retained in the interstitium, where it forms a dynamic reservoir via transient interactions with heparan sulfate proteoglycans (HSPGs). A membrane protein of capillary endothelial cells, glycosylphosphatidylinositol-anchored high-density lipoprotein binding protein 1 (GPIHBP1), captures LPL from the interstitial spaces and shuttles it across endothelial cells to the capillary lumen (4–6). Having reached the capillary lumen, the LPL–GPIHBP1 complex is the key functional unit for TRL processing, mediating both the docking of circulating TRLs to capillary endothelial cells (5) and the rapid hydrolysis of their triglyceride content (7). The resistance of LPL–GPIHBP1 complexes to inactivation by physiologic inhibitors [e.g., angiopoietin-like (ANGPTL) proteins 3, 4, and 8] serves to focus catalytically active LPL along the capillary lumen (8–13).

A wealth of genetic and experimental evidence highlights the importance of LPL and GPIHBP1 in maintaining normal plasma triglyceride levels. Homozygous or compound heterozygous loss-of-function mutations in *LPL* or *GPIHBP1* cause severe hypertriglyceridemia (familial chylomicronemia) (1, 2). This syndrome is associated with life-threatening bouts of acute pancreatitis (1). Also, mice with a deletion of *Gpihbp1* (*Gpihbp1*$^{-/-}$) or mice harboring a *Gpihbp1* missense mutation known to cause disease in humans (*Gpihbp1*$^{C63Y/C63Y}$) develop severe chylomicronemia (4, 14). In these mouse models, LPL remains confined within the interstitial spaces, never reaching the capillary lumen. Recent studies have shown that autoantibodies against GPIHBP1 cause some cases of acquired chylomicronemia (GPIHBP1 autoantibody syndrome) (15). GPIHBP1 autoantibodies bind to GPIHBP1 and block LPL binding, thereby abolishing the formation of the key functional unit (GPIHBP1–LPL) required for triglyceride hydrolysis within capillaries (15, 16).

To orchestrate the assembly of this functional unit, GPIHBP1 evolved unique structural properties (2). Despite being a relatively small protein (131 residues), GPIHBP1 is highly asymmetrical with an N-terminal intrinsically disordered region (IDR) rich in acidic residues, a disulfide-rich core Ly6/uPAR (LU) domain, and a short C-terminal region that tethers the protein to the cell membrane via a glycolipid anchor (2, 17). This multifaceted

Significance

Dietary fats absorbed by intestinal enterocytes are packaged into chylomicrons, which circulate in the bloodstream until docking along capillary endothelial cells, primarily in striated muscle and adipose tissue. There, a functional unit composed of lipoprotein lipase (LPL) and GPIHBP1 hydrolyzes the triglycerides in chylomicrons, releasing free fatty acids for use by surrounding parenchymal cells. The current study describes the interactions between LPL and GPIHBP1 and describes how a disordered region of GPIHBP1 results in order and functional stability within LPL. The elucidation of LPL–GPIHBP1 interactions sheds light on the regulation of intravascular triglyceride processing and provides insights into plasma triglyceride metabolism in health and disease.

Author contributions: K.K.K., S.G.Y., and M.P. designed research; K.K.K., S.M., O.K., L.G.F., and M.P. performed research; L.B.H., A.P.B., and G.O. contributed new reagents/analytic tools; K.K.K., S.R.M., S.M., O.K., N.S.-G., B.B.K., G.O., S.G.Y., T.J.D.J., L.G.F., and M.P. analyzed data; and K.K.K., S.G.Y., and M.P. wrote the paper.

Reviewers: J.D.H., University of Texas Southwestern Medical Center; and S.P., University of Central Florida.

Conflict of interest statement: S.G.Y. and Jay D. Horton were both principal investigators on a consortium grant. They did not collaborate directly.

[1]To whom correspondence may be addressed. Email: sgyoung@mednet.ucla.edu or m-ploug@finsenlab.dk.

This article contains supporting information online at www.pnas.org/lookup/suppl/doi:10.1073/pnas.1806774115/-/DCSupplemental.

Published online June 13, 2018.

structure plays different roles in the regulation of LPL activity in the capillary lumen. The folded LU domain is responsible for the formation of a stable complex with LPL, while the IDR stabilizes the hydrolase domain of LPL against spontaneous unfolding (12, 17). Nonetheless, only full-length GPIHBP1—and not the LU domain or the N-terminal IDR alone—efficiently protects LPL against ANGPTL4-catalyzed unfolding (12).

The concept that IDRs can regulate cellular functions via specific interactions emerged from studying intracellular proteins involved in cell signaling and nucleic acid binding (18). In this setting, specific phosphorylations in IDR sequences altered protein dynamics, adding a regulatory switch to IDR function (19, 20). The current study brings this concept—that IDRs can mediate specific protein interactions—into the realm of intravascular triglyceride metabolism (12, 17). First, we demonstrate that a conserved tyrosine within GPIHBP1's acidic IDR undergoes O-sulfation and that this modification affects LPL interactions and LPL stability. Second, we investigate the importance of the N-terminal acidic IDR for LPL binding, for stabilizing LPL activity, and for capturing LPL from the pool of HSPG-associated LPL within the subendothelial spaces. Finally, we assess the relevance of GPIHBP1's acidic IDR to the GPIHBP1 autoantibody syndrome, in which autoantibodies against GPIHBP1 block LPL binding and lead to severe chylomicronemia (15).

Results

Posttranslational Modifications of Human GPIHBP1. A secreted version of human GPIHBP1$^{1–131}$ was purified from the medium of transfected *Drosophila* S2 cells (17). The molecular mass of the principal protein species was 15,722.6 Da as determined by mass spectrometry (Fig. 1*A*, *Inset*). Posttranslational modifications accounted for 1,119 Da. N-glycanase treatment revealed that the GPIHBP1 contained one N-linked glycan (Fig. 1*A*), a typical biantennary glycan (21, 22) attached to Asn^{58} (*SI Appendix*, Fig. S1).

GPIHBP1 Carries a Tyrosyl-O-Sulfate Modification. After subtracting the mass of the N-linked glycan (1,038.96 Da), the mass of GPIHBP1 remained 80 Da greater than expected. This difference is compatible with one phosphorylation or sulfation. Only a minor fraction of GPIHBP1 lacked the 80-Da modification (Fig. 1*A*, *Inset*). The only posttranslational modification in a truncated human GPIHBP1 lacking the N-terminal acidic IDR (GPIHBP1$^{34–131}$) was the N-linked glycan (Table 1), strongly suggesting that the 80-Da modification is located within the first 33 residues of GPIHBP1. We verified that assignment by showing that the modification was present in a GPIHBP1$^{1–33}$ peptide released from full-length human GPIHBP1 with trypsin (Table 1). Peptide profiling narrowed the possible modification sites to residues 10–21, and Tyr^{18} was the only hydroxy-amino acid in that segment. To determine if Tyr^{18} was indeed the modification site, we created a GPIHBP1 mutant in which Tyr^{18} was replaced by phenylalanine (GPIHBP1$^{1–131/Y18F}$). This single amino acid substitution eliminated the 80-Da modification in GPIHBP1 (Table 1).

Several lines of evidence showed that Tyr^{18} in GPIHBP1 carries a sulfate rather than a phosphate. First, phosphorylated, but not sulfated, versions of GPIHBP1$^{1–33}$ peptides were sensitive to phosphatase (*SI Appendix*, Fig. S2 *A–D*), and GPIHBP1$^{1–33}$ that had been released from GPIHBP1$^{1–131}$ with trypsin was resistant

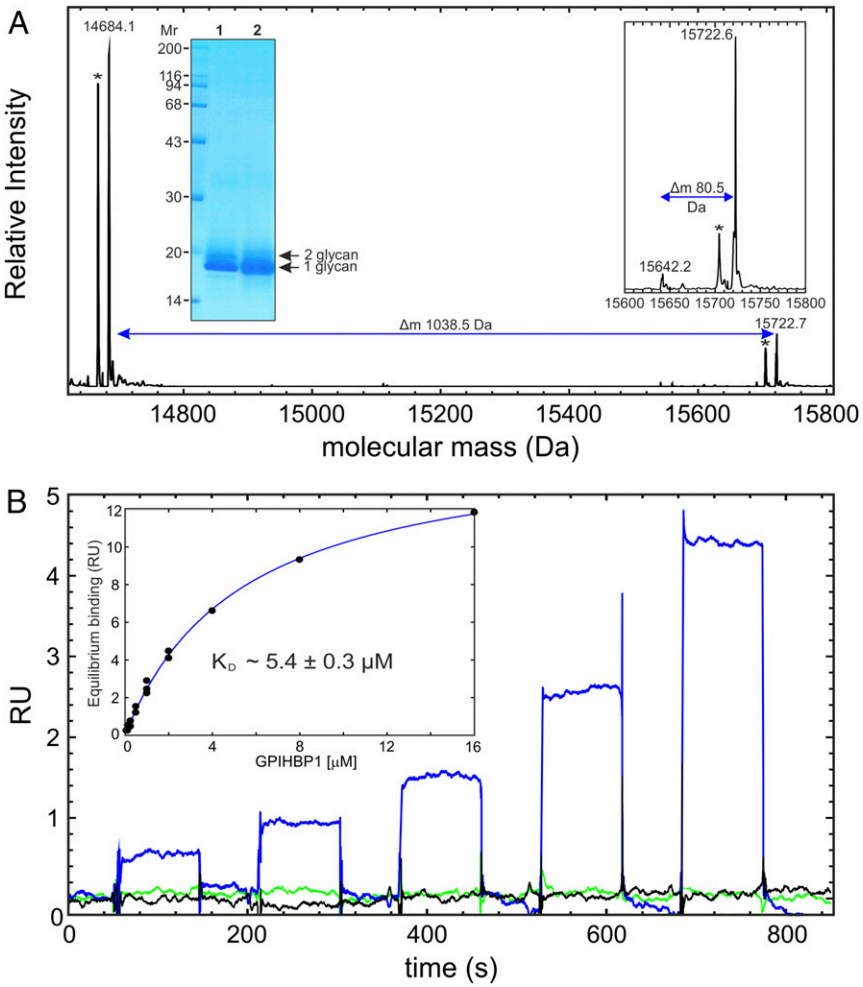

Fig. 1. Posttranslational modifications of recombinant human GPIHBP1. (*A*) Human GPIHBP1$^{1–131}$ produced in *Drosophila* S2 cells was analyzed by SDS/PAGE and Coomassie blue staining (nonreduced, lane 1; reduced and alkylated, lane 2). Mass spectra are shown for intact GPIHBP1 before (*Inset*) and after N-glycanase treatment under native conditions, which reduces the molecular mass by 1,038.5 Da corresponding to one paucimannosidic N-glycan with a core fucose ($Man_3GlcNAc_2Fuc$), the archetypical insect cell glycan (21). The asterisks indicate the loss of 17 Da due to the formation of pyroglutamate at the N-terminal glutamine in human GPIHBP1. (*B*) Sensorgrams showing the interactions between immobilized anti-sulfotyrosine mAb 1C-A2 (1,280 RU) and GPIHBP1$^{1–131}$ (blue curve), GPIHBP1$^{1–131/Y18F}$ (green curve), and buffer (black curve). The SPR sensorgrams were recorded with a BiacoreT200 instrument and are shown for sequential injections of twofold dilutions of GPIHBP1 from 125 nM to 2 μM without intervening regenerations. The affinity between GPIHBP1$^{1–131}$ and mAb 1C-A2 was 5.4 μM (determined from several runs up to 16 μM GPIHBP1; see *Inset*).

MEDICAL SCIENCES

Table 1. Mass spectrometry characterization of GPIHBP1

GPIHBP1	Mass, Da	Recorded mass, Da	Δmass, Da
1–131	14,603.66	15,722.6	80.1
		15,642.2	−0.4
$1–131^{degly}$	14,604.64	14,684.1	79.5
34–131	10,579.91	11,619.2	0.3
$1–131^{Y18F}$	14,587.66	15,627.0	0.1
1–33	4,039.48	4,119.41*	79.93

Protein masses were recorded on a Synapt G2 mass spectrometer (Waters), and the average molecular masses were calculated by MaxEnt deconvolution. The mass difference (Δ mass) was calculated after subtracting the mass of the glycan on Asn^{58} (1,038.96 Da). Note: both GPIHBP1 and GPIHBP^{Y18F} contain the R38G mutation to increase protein purification yields.
*The monoisotopic mass for GPIHBP$1^{1–33}$, released from intact GPIHBP1 by trypsin, was calculated from the $(M+4H)^{4+}$ charge state.

to phosphatase (*SI Appendix*, Fig. S2 *E* and *F*). Second, a monoclonal anti–Tyr-OSO_3 antibody (1C-A2) (23) bound to purified GPIHBP$1^{1–131}$ but not to GPIHBP$1^{1–131/Y18F}$ (Fig. 1*B*). Third, Sulfinator (24) and GPS-TSP (25) programs identified Tyr^{18} as a likely sulfation site (*SI Appendix*, Fig. S3).

Alignments of GPIHBP1 sequences from different phylogenetic orders of Mammalia revealed an N-terminal IDR that was invariably present and enriched in acidic residues, although the amino acid sequence varied considerably (*SI Appendix*, Fig. S3). The tyrosyl-O-sulfation site (i.e., Tyr^{18} in mature human GPIHBP1) was largely invariant, with only a few exceptions (e.g., members of the Equidae family). To determine if the conserved tyrosine was sulfated in the GPIHBP1 of other mammalian species, we expressed mouse GPIHBP1, excised the acidic peptide with trypsin, and then confirmed by mass spectrometry that the acidic peptide was sulfated (*SI Appendix*, Fig. S2 *G* and *H*).

Stoichiometry and Affinity of LPL Binding to GPIHBP1. To define the stoichiometry of the LPL–GPIHBP1 interaction, we incubated 3 μM LPL with increasing concentrations of intact GPIHBP$1^{1–131}$ or the disordered polypeptide GPIHBP$1^{1–33}$ (at concentrations above the K_d). We chose native PAGE to assess LPL–GPIHBP1 complex formation because of the large differences in pI values and molecular masses of the two proteins (9.5 and 50.5 kDa, respectively, for LPL vs. 4.1 and 15.7 kDa, respectively, for GPIHBP1). The titration resulted in the formation of an LPL–GPIHBP1 complex with a distinct electrophoretic mobility (Fig. 2). Scanning of Coomassie blue-stained bands revealed that the stoichiometry of the LPL–GPIHBP1 complex was 1:1, regardless of whether the titrations involved GPIHBP$1^{1–131}$ (Fig. 2*A*), GPIHBP$1^{1–33}$ (Fig. 2*B*), or GPIHBP$1^{1–131/Y18F}$ (Fig. 2*C*).

To assess the impact of tyrosyl-O-sulfation on the kinetics of LPL binding, we measured the association (k_{on}) and dissociation (k_{off}) rate constants between GPIHBP1 in solution and LPL captured on the LPL-specific monoclonal antibody 5D2. Using surface plasmon resonance (SPR) and single-cycle kinetics, we found that the rate constants for GPIHBP$1^{1–131}$ and 5D2-captured LPL were fast i.e., $k_{on} > 10^7\ M^{-1}\ s^{-1}$ (Fig. 2*D*). A parallel analysis of GPIHBP$1^{1–131/Y18F}$ revealed a threefold increase in K_d, a consequence of changes in both k_{on} and k_{off} (Fig. 2*E*). This difference persisted when the rate constants were measured on different days with different protein preparations and different sensor chips (Table 2).

To confirm this finding with an orthogonal method, we used microscale thermophoresis (MST) to assess the impact of Tyr^{18} modifications on the capacity of synthetic GPIHBP$1^{1–33}$ peptides to inhibit equilibrium binding between LPL and GPIHBP$1^{1–131}$ (Fig. 2*F*). In keeping with the SPR results (Fig. 2 *D* and *E*), the inhibitory potential was greatest for GPIHBP$1^{1–33}$ peptides in which Tyr^{18} was sulfated or phosphorylated (IC_{50} 0.3 μM) and lower for peptides containing unmodified Tyr^{18}, Phe^{18}, or Glu^{18} (IC_{50} 0.6–0.7 μM).

The impact of GPIHBP1's acidic IDR on LPL binding is best illustrated by the fact that the LPL–GPIHBP1 encounter rate is >250-fold greater with GPIHBP$1^{1–131}$ (k_{on} $2.5 \times 10^7\ M^{-1}\ s^{-1}$) than with a truncated GPIHBP$1^{34–131}$ (k_{on} $0.008 \times 10^7\ M^{-1}\ s^{-1}$). This difference represents a conservative estimate, given that mass-transport limitations is more pronouncedly slowing interactions driven by very fast k_{on} in SPR analyses. Extrapolation from experiments conducted at higher ionic strengths suggested that the actual k_{on} for the GPIHBP$1^{1–131}$–LPL interaction is at least 10-fold faster (i.e., $3 \times 10^8\ M^{-1}\ s^{-1}$) at 150 mM NaCl (Fig. 2*G*). It is likely that electrostatic forces between charged surfaces drive this fast association rate (i.e., the acidic IDR in GPIHBP1 and the basic heparin-binding motifs in LPL) (26). Increasing ionic strength increases K_d primarily by decreasing k_{on}, with only a minor impact on k_{off} (Fig. 2*G* and Table 2); these effects are a hallmark of interactions controlled by electrostatic steering (27, 28).

Protecting Against ANGPTL4-Catalyzed LPL Unfolding with GPIHBP1. We showed previously that the N-terminal acidic IDR in GPIHBP1 protects LPL from spontaneous and ANGPTL4-catalyzed unfolding and inactivation (12, 17). To measure the relevance of the Tyr^{18}-OSO_3 modification in this process, we used the same pulse-labeled hydrogen–deuterium exchange/mass spectrometry (HDX-MS) protocol that we developed to assess LPL unfolding (12, 17). In brief, 10 μM LPL was incubated with 2 μM ANGPTL4$^{1–159}$ for 10 min at 25 °C in protiated solvents followed by a 10-s pulse labeling in 70% D_2O. Based on the bimodal isotope envelopes for LPL peptide 131–165, we found that free LPL undergoes extensive (>85%) unfolding under these conditions (12, 17). Including 30 μM GPIHBP$1^{1–131}$ during the LPL/ANGPTL4 incubation reduced LPL unfolding to 8 ± 2%. Under identical conditions, the protection provided by 30 μM GPIHBP$1^{1–131/Y18F}$ was blunted (14 ± 1% unfolding of LPL) (Fig. 3*A*). GPIHBP$1^{1–33}$ peptides alone provided much lower degrees of protection (12), but there was a similar trend: GPIHBP$1^{1–33}$ peptides that were sulfated or phosphorylated were more potent in protecting LPL from ANGPTL4-mediated unfolding (Fig. 3*B*). Because these experiments were conducted at concentrations far exceeding the K_d for GPIHBP1–LPL interactions, our results suggest that O-sulfation of Tyr^{18} assists in protecting LPL against ANGPTL4-catalyzed unfolding.

When we measured the catalytic activity of LPL in the setting of more physiological concentrations of LPL, the effects of the Tyr^{18}-OSO_3 modification were also apparent. Incubating 15 nM LPL with 15 nM ANGPTL4 in the absence of GPIHBP1 potently inactivated LPL, leaving only 8 ± 3% residual LPL activity. When 15 nM GPIHBP$1^{1–131}$ was included in the incubation, LPL activity was protected (38 ± 2% residual activity). When we used 15 nM GPIHBP$1^{1–131/Y18F}$, protection of LPL was diminished (22 ± 3% residual activity) (Fig. 3*C*). Two factors are likely to contribute to the reduced efficiency of GPIHBP$1^{1–131/Y18F}$ in protecting LPL: (*i*) a weaker affinity for LPL and (*ii*) attenuated protection of LPL from the absence of the sulfated tyrosine within the acidic IDR (Fig. 3*A*). We suspect that the latter effect is dominant because we also observed significant differences in the ability of GPIHBP$1^{1–131}$ and GPIHBP$1^{1–131/Y18F}$ to protect LPL when those proteins were added to the incubation mixture at concentrations as high as 300 nM (82 ± 2% with GPIHBP$1^{1–131}$ vs. only 71 ± 3% with GPIHBP$1^{1–131/Y18F}$).

Transitioning of LPL from an HSPG–Bound State to a Complex with GPIHBP1. GPIHBP1-mediated extraction of LPL from interstitial HSPG binding sites represents an important step in the transit of LPL to the capillary lumen (6). Earlier confocal immunofluorescence microscopy studies on tissues from wild-type mice showed that GPIHBP1 and LPL are present at the apical (luminal) and basolateral surfaces of capillaries, whereas the LPL in *Gpihbp1*$^{-/-}$ mice never reaches the capillary lumen and instead remains bound to HSPGs in close proximity to the surface of cells, including both parenchymal and endothelial cells (2, 6). We

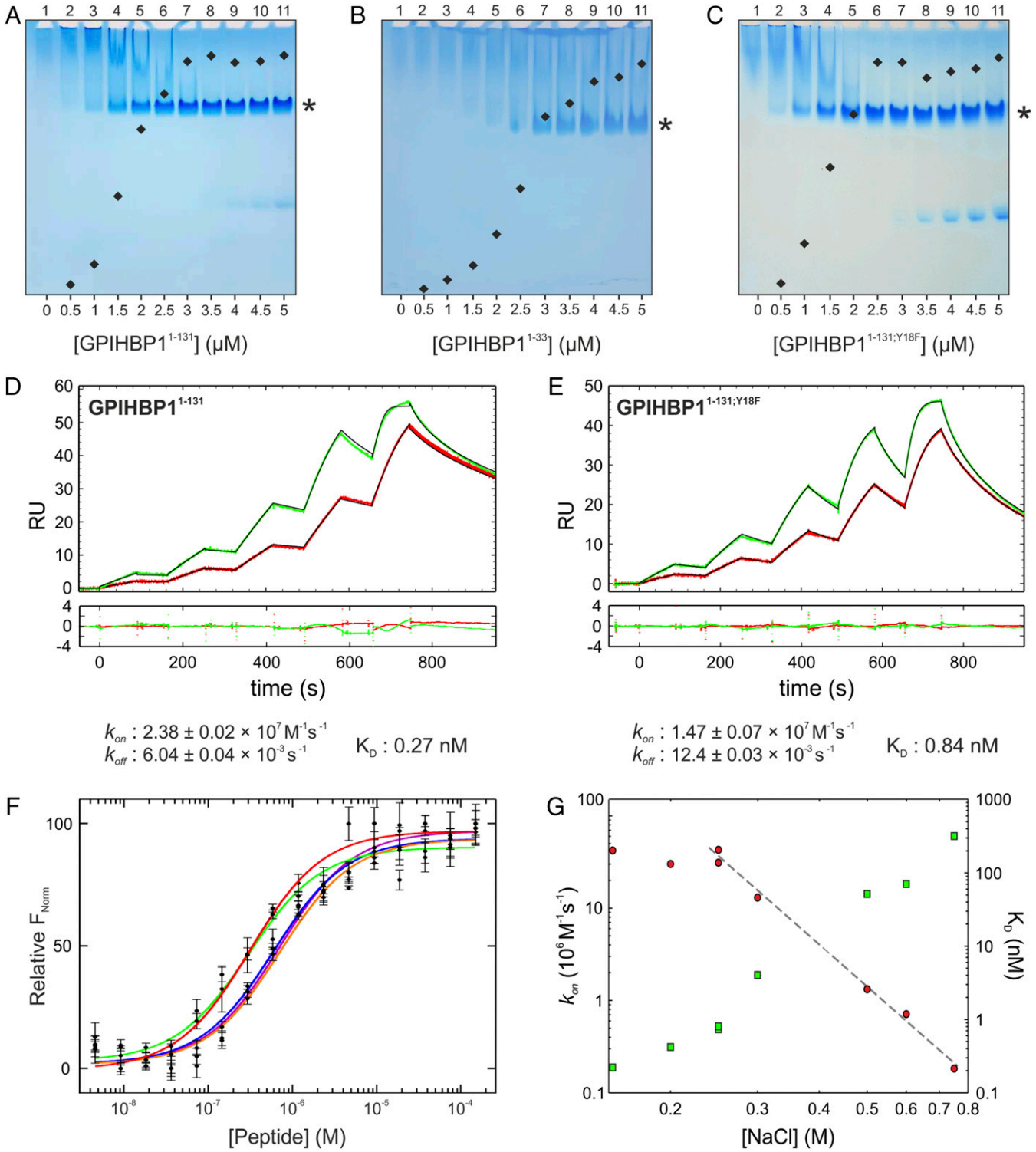

Fig. 2. Binding stoichiometry and affinity of LPL–GPIHBP1 complexes. (*A*–*C*) The binding stoichiometry between LPL and GPIHBP1 was determined by native PAGE titrating 3 μM LPL (lane 2) with increasing amounts of GPIHBP1 ligand (range, 0.5–5.0 μM) (lanes 3–11). The relative amounts of LPL–GPIHBP1 complexes (marked by asterisks) were determined by scanning the Coomassie blue-stained bands and are superimposed as black diamonds. Data for GPIHBP1$^{1-131}$ and GPIHBP1$^{1-33}$ (both with Tyr^{18}-OSO$_3$) and GPIHBP1$^{1-131/Y18F}$ are shown in *A*–*C*, respectively. (*D* and *E*) Single-cycle kinetics with SPR for the interactions between LPL captured on mAb 5D2 and twofold dilutions of GPIHBP1$^{1-131}$ (*D*) or GPIHBP1$^{1-131/Y18F}$ (*E*). Shown are two single-cycle runs of five GPIHBP1 concentrations ranging from 0.125–2 nM (red curves) or 0.25–4 nM (green curves). Data were fit to a simple bimolecular interaction (black curves) with the derived kinetic constants and the residuals shown beneath the sensorgrams. (*F*) Inhibitory capacity of synthetic GPIHBP1$^{1-33}$ peptides on the LPL–GPIHBP1$^{1-131}$ interaction as assessed by MST. The following peptides were measured: unmodified (orange, IC_{50} 0.71 ± 0.20 μM); Tyr^{18}-OSO$_3$ (red, IC_{50} 0.31 ± 0.05 μM); Tyr^{18}–OPO$_3$ (green, IC_{50} 0.30 ± 0.05 μM); Tyr^{18}Phe (blue, IC_{50} 0.60 ± 0.16 μM); and Tyr^{18}Glu (purple, IC_{50} 0.70 ± 0.08 μM). Each titration shows results from four independent replicates. Titrations with Tyr^{18} are significantly different from those with Tyr^{18}-OSO$_3$ ($P < 0.01$, Student's *t* test). (*G*) Impact of ionic strength on K_d (green squares) and k_{on} (red circles) for the LPL–GPIHBP1$^{1-131}$ interaction as assessed by SPR.

Table 2. GPIHBP1 binding kinetics to LPL

GPIHBP1	k_{on}, 10^6 M^{-1} s^{-1}	k_{off}, 10^{-2} s^{-1}	K_d, nM	R_{max}, fmol/mm^2	*n*
GPIHBP1$^{1\text{-}131}$	26.5 ± 8.2	1.26 ± 0.03	0.53 ± 0.14	1.59 ± 0.19	10
GPIHBP1$^{1–131;Y18F}$	16.7 ± 6.4	1.81 ± 0.06	1.19 ± 0.30	1.40 ± 0.13	10
GPIHBP1$^{34–131}$	0.087 ± 0.035	0.73 ± 0.31	97.5 ± 54.3	1.62 ± 0.06	5
GPIHBP1$^{1–131}$ *(0.30 M NaCl)*	13.0 ± 0.59	5.25 ± 0.25	4.0		1
GPIHBP1$^{1–131}$ *(0.50 M NaCl)*	1.36 ± 0.04	6.82 ± 0.12	52		1
GPIHBP1$^{1–131}$ *(0.75 M NaCl)*	0.18 ± 0.01	5.81 ± 0.03	317		1

Kinetic rate constants (k_{on} and k_{off}) were derived by global fitting of sensorgrams recorded by five consecutive single-cycle injections of GPIHBP1 on LPL that had been captured by mAb 5D2. The values shown are means ± SDs for single-cycle analyses performed on different chips, preparations, and days. We obtained a uniform capture level of LPL corresponding to 150 RU (approximately 3 fmol/mm^2).

speculated that GPIHBP1 would be most effective in capturing LPL if the LPL bound preferentially to the HSPGs on endothelial cells. To explore that hypothesis, we performed additional confocal microscopy studies on the heart and skeletal muscle of *Gpihbp1*$^{-/-}$ mice. Once again, we found that LPL was mislocalized within the interstitial spaces. However, we also noted that LPL associated preferentially with endothelial cells compared with parenchymal cells of the heart even in the absence of GPIHBP1 (Fig. 4 and *SI Appendix*, Fig. S4). This scenario was also evident in skeletal muscle (gastrocnemius) (Fig. 5*A* and *SI Appendix*, Fig. S5). We suspect that the preferential binding of LPL to endothelial cells could reflect higher levels of HSPG sulfation in capillary endothelial cells. HSPG composition is known to vary among different organs and tissues (29–31), and this could influence LPL binding (32, 33). To pursue the idea that different levels of HSPG sulfation could affect the transitioning of LPL to GPIHBP1, we tested the ability of different heparin preparations (with defined length but variable sulfation patterns) to interfere with GPIHBP1–LPL interactions. As shown in Fig. 5*B*, removal of N-sulfate, 2-O-sulfate, or 6-O-sulfate affected the capability of these defined heparin derivatives to inhibit the GPIHBP1–LPL interaction. These studies raise the possibility that the LPL associated with HSPGs (e.g., glypicans, syndecans) on the surface of parenchymal cells gradually moves to higher-affinity HSPGs on capillary endothelial cells [i.e., resembling the mechanism of directed diffusion established for some HSPG-tethered morphogens (34)]. Once LPL reaches the basolateral surface of capillaries, GPIHBP1 would capture LPL and escort it across endothelial cells to the capillary lumen.

To investigate the role of GPIHBP1's acidic IDR on the movement of LPL to the basolateral surface of capillary endothelial cells, we developed an SPR sensor surface that models the

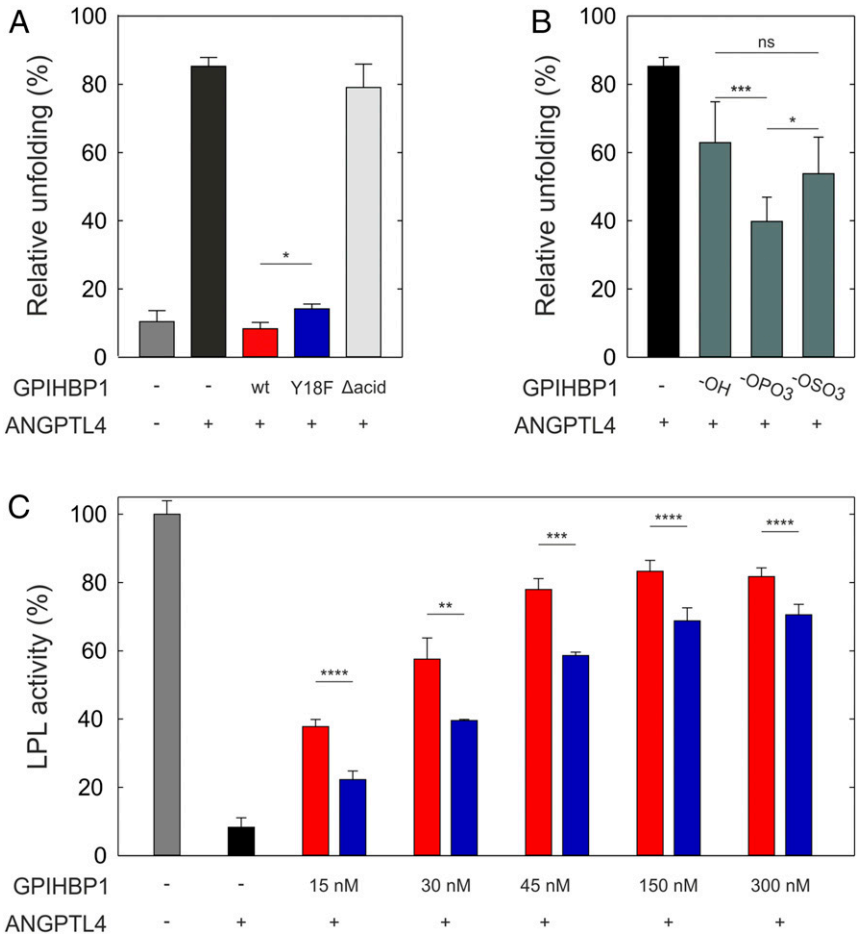

Fig. 3. Mitigation of ANGPTL4-mediated LPL unfolding and inactivation by GPIHBP1. (*A*) We measured LPL unfolding with HDX-MS by quantifying the bimodal distribution of the isotope envelopes for the LPL peptide 131–165 (containing Ser^{134} and Asp^{158} of the catalytic triad). Relative amounts of unfolding of 10 μM LPL incubated for 10 min at 25 °C alone (gray bar) or in the presence of 2 μM ANGPTL4$^{1–159}$ (black bar) are shown. Incubations with ANGPTL4 were also performed with 30 μM GPIHBP1$^{1–131}$ (wt, red bar); 30 μM GPIHBP1$^{1–131;Y18F}$ (*Y18F*, blue bar), or 30 μM GPIHBP1$^{34–131}$ (*Δacid*, light gray bar). (*B*) Impact of 30 μM GPIHBP1$^{1–33}$ in a similar setting with Tyr^{18} being unmodified (-OH), phosphorylated (-OPO_3), or sulfated (-OSO_3). (*C*) Catalytic activity of 15 nM LPL alone (100% corresponding to 51.9 U/mL) or in the presence of 15 nM ANGPTL4$^{1–159}$. These incubations were performed with 15, 30, 45, 150, or 300 nM GPIHBP1$^{1–131}$ (red bars) or GPIHBP1$^{1–131;Y18F}$ (blue bars). Numbers of replicates for each experiment range from 3 to 12. Comparison of data with an unpaired *t* test: *$P \leq 0.05$; **$P \leq 0.01$; ***$P \leq 0.001$; ****$P \leq 0.0001$; ns, not significant.

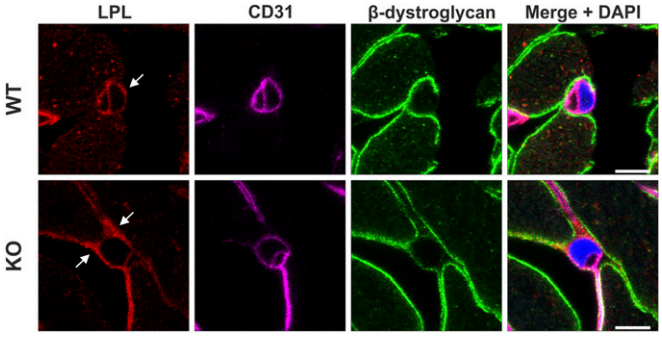

Fig. 4. Localization of LPL in the mouse heart. The distribution of LPL in the hearts of wild-type and *Gpihbp1*$^{-/-}$ (KO) mice was assessed by immunohistochemistry with antibodies against LPL (red), CD31 (magenta), or β-dystroglycan (green). Nuclei were stained with DAPI (blue). Shown are confocal fluorescence microscopy images of capillary endothelial cells containing an endothelial cell nucleus (which makes it possible to visualize the basolateral and apical membranes). In the wild-type mouse heart, LPL was associated almost exclusively with capillary endothelial cells (arrow). In the heart of a *Gpihbp1*-deficient mouse, the LPL is mislocalized within the interstitial spaces surrounding both myocytes and capillary endothelial cells, but LPL appeared to bind in close proximity to capillary endothelial cells (arrows). (Scale bars, 5 μm.)

dynamic state of LPL–HSPG interactions in the subendothelial spaces and the transitioning of that pool of LPL to GPIHBP1 on the basolateral surface of capillaries. In this model, LPL binds to a high-density surface of heparin fragments (300 fmol/mm^2) on the sensor chip. The retention of LPL on this surface is largely governed by mass transport limitations, with any LPL dissociation event quickly followed by the binding of LPL to an adjacent unoccupied heparin. Injection of GPIHBP1 over the surface would allow any unbound LPL to interact with GPIHBP1. If the newly formed LPL–GPIHBP1 complexes no longer bind to the sensor surface, they would be removed by the buffer flow. We predict that this in vitro system resembles the movement of LPL from HSPGs in the subendothelial space to GPIHBP1 on the basolateral surface of capillaries, a binding event that promptly leads to shuttling of the LPL–GPIHBP1 complex to the capillary lumen. Our SPR system revealed that intact GPIHBP1 efficiently extracted LPL from the heparin-bound pool on the sensor chip (Fig. 5*C*). Although injections of GPIHBP1$^{34–131}$ led to LPL binding, those binding events were not accompanied by accelerated removal of LPL from heparin. Thus, the presence of the acidic IDR was decisive for a GPIHBP1-mediated LPL mobilization from heparin. Posttranslational modification with Tyr^{18}-OSO_3 improved the function of GPIHBP1 in this process, as GPIHBP1$^{1–131/Y18F}$ resulted in significantly lower levels of LPL mobilization (Fig. 5*C*).

Space Occupied by the Acidic IDR of GPIHBP1. Although the physiologic importance of GPIHBP1 is well established, the structure of GPIHBP1 has not been determined. Using small-angle X-ray scattering (SAXS), we found that GPIHBP1$^{1–33}$ adopts a flexible, disordered, and extended conformation at pH 7.4 in 136 mM NaCl with a maximum dimension (D_{max}) of 65 Å and a gyration radius (R_g) of 19.8 Å (Fig. 6 *A*–*C* and *SI Appendix*, Table S1). We observed no significant difference in the scattering profiles of GPIHBP1$^{1–33}$ peptides containing Tyr^{18}-OSO_3 and Tyr^{18}-OPO_3, indicating that those modifications do not induce pronounced shifts in the ensemble.

To obtain information on the flexibility of the acidic domain in the context of GPIHBP1, we examined both GPIHBP1$^{34–131}$ and GPIHBP1$^{1–131}$ by combining in-line size-exclusion chromatography with SAXS (SEC-SAXS). The scattering data for GPIHBP1$^{34–131}$ (Fig. 6*E*) provided a suboptimal match to our model for the LU domain in GPIHBP1 (17) (CRYSOL; χ^2 4.6). By adjusting for the flexibility of the small biantennary glycan on Asn^{58} [with the AllosMod-FoXS server (35)], a moderately improved fit was obtained (χ^2 3.9). Guided by earlier HDX-MS analyses (17), we allowed flexibility in certain regions of the peptide backbone of the GPIHBP1$^{34–131}$ model (Fig. 6*D*). Applying the ensemble optimization method (EOM) for this condition led to a substantial improvement in the fit (χ^2 2.4). Superimposing all ensembles selected during 10 separate rounds of EOM revealed that the C-terminal region of GPIHBP1 (residues 113–131) projected away from the central β-sheet of GPIHBP1$^{34–131}$ (Fig. 6*E* and *SI Appendix*, Table S3). Of note, this orientation is recapitulated by independent EOM analysis with intact GPIHBP1$^{1–131}$ (Fig. 6*G*). These data imply that GPIHBP1 projects its LPL-binding interface [defined by HDX-MS and site-directed mutagenesis (17, 36)] away from the cell surface.

Fitting the scattering data for full-length GPIHBP1$^{1–131}$ with the EOM revealed that the acidic domain occupies a large mushroom-shaped space with a diameter of 112 Å (Fig. 6 *F* and *G*). This prediction aligns well with the scattering data for GPIHBP1$^{1–33}$ peptides, which exhibit a D_{max} of 65 Å. From a functional perspective, we propose that the large space occupied by the acidic IDR is important for recruiting LPL from the subendothelial HSPG binding sites via long-range electrostatic steering, facilitating a subsequent high-affinity interaction with GPIHBP's LU domain.

Reactivity of GPIHBP1 Autoantibodies. Due to their low sequence complexity and paucity of hydrophobic residues, IDRs are generally poor ligands for MHC class II and are likely to escape adaptive immune responses (37, 38). In keeping with our SAXS data, the first 35 residues of human GPIHBP1 are predicted to be highly disordered, translating into a low predicted affinity for MHC class II (Fig. 7*A*). Despite these considerations, a mouse monoclonal antibody against human GPIHBP1 (mAb RF4) was proposed to bind a linear epitope within GPIHBP1's acidic domain (based on the observation that the antibody bound to full-length GPIHBP1 but not to a mutant lacking the acidic domain) (39). Because IDRs such as GPIHBP1's acidic domain are not expected to elicit a strong immune response, we revisited the location of the mAb RF4 epitope. With SPR, we compared the kinetics of mAb RF4 binding to synthetic peptides derived from the acidic IDR of GPIHBP1. Our studies mapped the epitope for mAb RF4 to residues 27–44 within GPIHBP1, with Arg^{33} and Leu^{34} being the hot-spot residues, and those residues are not conserved in mouse GPIHBP1 (Fig. 7 *B* and *C* and *SI Appendix*, Fig. S6). Thus, the epitope for RF4 is located downstream from the acidic IDR, in the region just upstream of the folded LU domain (arrow in Fig. 7*A*).

We recently reported that some patients develop chylomicronemia as a result of GPIHBP1 autoantibodies that block LPL binding (GPIHBP1 autoantibody syndrome) (15, 16). To assess the involvement of the IDR in this disease, we captured antibodies from an affected patient on a Protein G sensor chip. Injections of GPIHBP1 revealed that 2.2 ± 0.3% of the patient's IgGs bound to GPIHBP1 (Fig. 7*D*). In keeping with that result, affinity purification of the total IgG fraction on a human GPIHBP1–Sepharose column resulted in a 1.2% yield of antibodies recognizing GPIHBP1. When analyzed by SPR, the immunopurified autoantibodies bound with high affinity to GPIHBP1$^{34–131}$, whereas there was no binding to GPIHBP1$^{1–45}$ (Fig. 7*E*). The same properties (binding to GPIHBP1$^{34–131}$ but not to GPIHBP1$^{1–45}$) were observed with the IgGs purified from the plasma of a second patient with the GPIHBP1 autoantibody syndrome (*SI Appendix*, Fig. S7). These findings support the idea that GPIHBP1's acidic domain is not immunogenic and that autoantibodies against the acidic domain are not relevant to the pathogenesis of this autoimmune chylomicronemia syndrome.

Discussion

GPIHBP1 plays at least three distinct roles in the intravascular processing of triglyceride-rich lipoproteins. First, GPIHBP1 binds LPL in the subendothelial spaces and shuttles it to its site of action in the capillary lumen (6). Second, GPIHBP1–LPL complexes in capillaries mediate the margination of chylomicrons along capillaries (5). Third, GPIHBP1 protects LPL from two physiologic inhibitor

MEDICAL SCIENCES

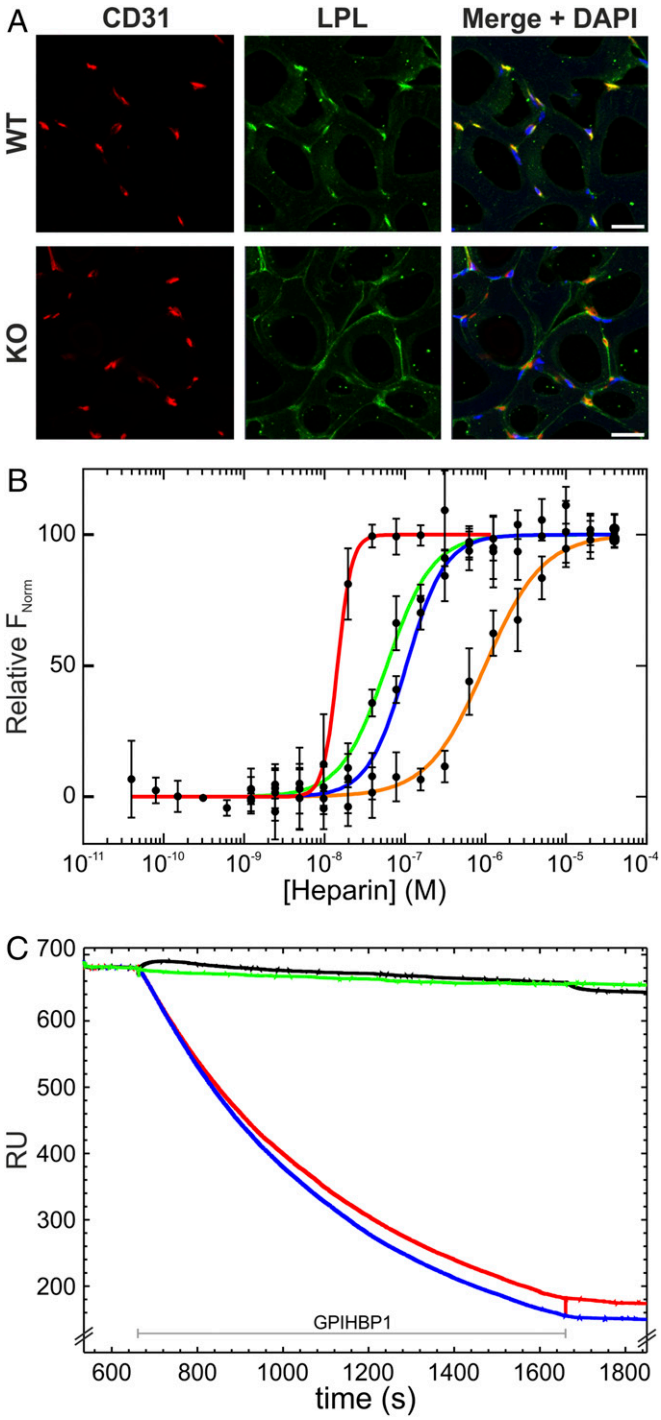

Fig. 5. Movement of LPL between HSPGs and GPIHBP1. (*A*) The distribution of LPL in gastrocnemius muscle of wild-type and *Gpihbp1*$^{-/-}$ (KO) mice was assessed by confocal immunofluorescence microscopy with antibodies against LPL (green) and CD31 (red). Nuclei were stained with DAPI (blue). In the wild-type mouse LPL was associated almost exclusively with capillary endothelial cells. In the *Gpihbp1*-deficient mouse the LPL is mislocalized within the interstitial spaces surrounding both myocytes and capillary endothelial cells, but LPL appeared to bind preferentially to capillary endothelial cells. (Scale bars, 20 μm.) (*B*) Competition of the GPIHBP1–LPL interaction by defined heparin fragments (dp10) by MST. Heparin (red curve; IC_{50} <14 nM), desulfated on the C2 oxygen of iduronate (green curve; IC_{50} 59 ± 5 nM), desulfated on the C6 oxygen of glucosamine (blue curve; IC_{50} 100 ± 10 nM), and desulfated on the C2 amine of glucosamine (orange curve; IC_{50} 980 ± 14 nM). (*C*) Mobilization of LPL from a high-density heparin surface by the injection of 200 nM of various GPIHBP1 derivatives. After 1,000-s exposures of GPIHBP1 at a flowrate of 20 μL/min (gray line), different levels of LPL remained on the heparin surface: 23.1% by GPIHBP1$^{1–131}$ (blue curve); 27.3% by GPIHBP1$^{1–131;\ Y18F}$ (red curve); and 97.0% by GPIHBP1$^{34–131}$ (black curve). Although the difference between GPIHBP1$^{1–131}$ and GPIHBP1$^{1–131;\ Y18F}$ was modest (2.5 ± 1.6%), it was highly significant when comparing 10 consecutive runs with a paired *t* test ($P < 0.001$). Buffer control is shown by the green curve.

proteins, ANGPTL3 and ANGPTL4 (12, 17). The acidic IDR within GPIHBP1, the focus of the current studies, contributes to the regulation of plasma triglyceride metabolism at all three levels.

We now demonstrate that electrostatic steering boosts the encounter rate between GPIHBP1 and LPL, increasing the association rate constant by >250-fold, a finding that is likely relevant to the interactions between GPIHBP1 and LPL in the subendothelial spaces. The acidic IDR in GPIHBP1 is the key factor in driving the accelerated kinetics of LPL binding and almost certainly does so by transient interactions with LPL's basic heparin-binding regions. Our SAXS analyses revealed that GPIHBP1's acidic IDR spans a relatively large conformational space (112 Å in diameter), which likely augments its capacity to capture LPL within the subendothelial spaces. We also documented the existence of a hitherto unrecognized tyrosyl-O-sulfation near the center of GPIHBP1's IDR and showed that this modification slightly increases the affinity of GPIHBP1–LPL interactions. We expect that the combined impact of these biochemical properties renders GPIHBP1 highly adept for extracting LPL from its HSPG-tethered reservoir in the subendothelial spaces. The importance of GPIHBP1's IDR in recruiting LPL to GPIHBP1 is supported by the observation that full-length GPIHBP1 removes LPL from heparin on SPR sensor chips, whereas GPIHBP1$^{34–131}$ does not. We speculate that GPIHBP1's acidic IDR is crucial for extracting LPL from the subendothelial spaces, explaining why this domain has been so strongly conserved during mammalian evolution.

With a view to LPL partitioning in the subendothelial spaces of myocytes, we observed by confocal immunofluorescence microscopy that LPL accumulates in close proximity to the capillary endothelial cells of heart and skeletal muscle even when GPIHBP1 is absent. This finding implies directional movement of interstitial LPL to capillary endothelial cells. The mechanism underlying directional movement to endothelial cells is unknown, but we suspect that the mechanism involves the same general factors shaping the concentration gradients of morphogens during tissue differentiation and embryogenesis (34, 40, 41). In the latter process, the density and sulfation profile of HSPGs are important factors, along with extracellular processing of HSPGs by secreted endosulfatases (42). In triglyceride metabolism, HSPGs were for many decades considered the primary binding site for LPL within the capillary lumen (43), and there was little discussion of HSPGs in the subendothelial spaces. Subsequent studies showed that GPIHBP1, not HSPGs, is the binding site for LPL inside capillaries (4–6). Interestingly, those same studies cast a spotlight on the relevance of subendothelial HSPGs in LPL trafficking. In GPIHBP1-deficient mice, the newly secreted LPL is not removed from the subendothelial spaces by lymph drainage but remains bound, via a transient interaction with HSPGs. The current studies add to our understanding of LPL interactions within the interstitium. In GPIHBP1-deficient mice, LPL associates preferentially with capillaries, implying that LPL moves in a directional fashion from the HSPGs surrounding parenchymal cells to HSPGs near capillary endothelial cells. Collagen XVIII and perlecan are the two major HSPGs found in vascular basement membranes. We would not be surprised if collagen XVIII plays a role in the directional movement of LPL toward capillaries, because *Col18a1*$^{-/-}$ mice have increased plasma triglyceride levels along with reduced transport of LPL to the capillary lumen (44).

The LPL–GPIHBP1 complex in the capillary lumen is required for margination of TRLs along capillaries. This docking process occurs despite vascular shear stress and resembles the

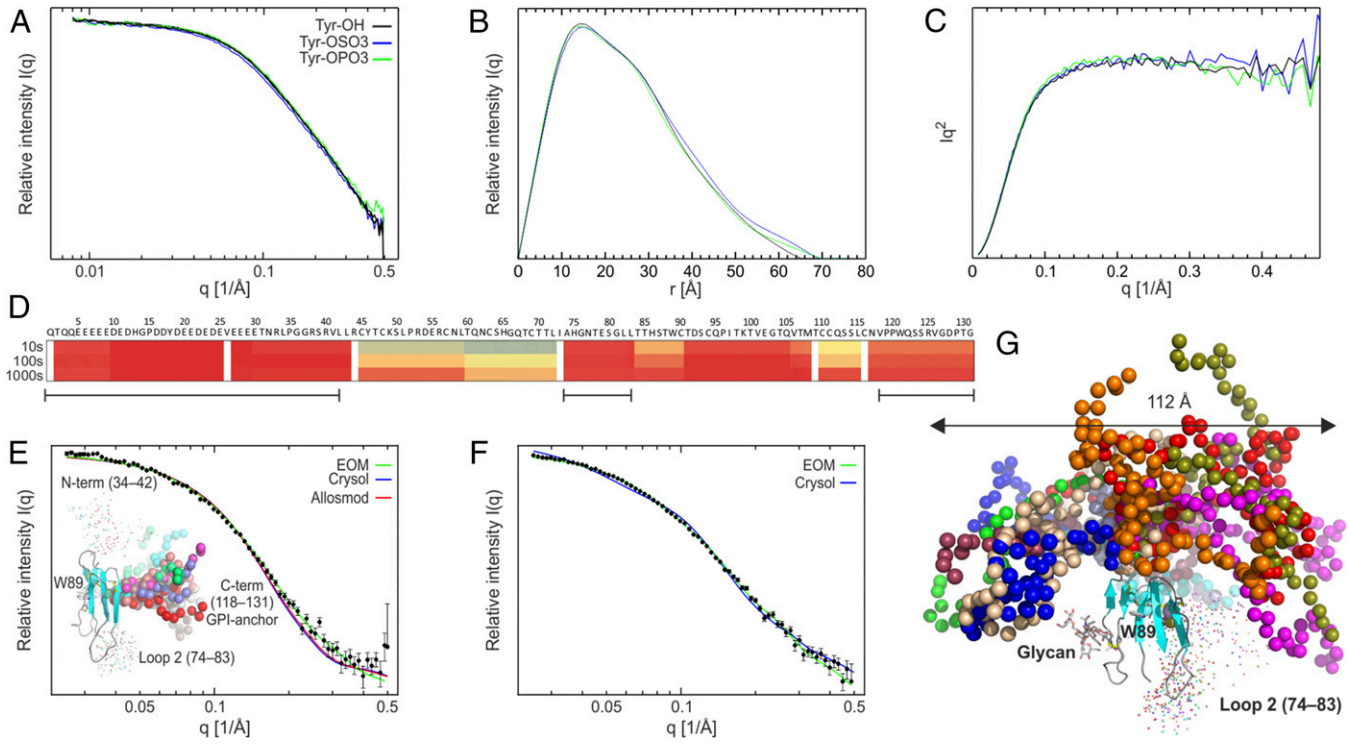

Fig. 6. SAXS analyses of GPIHBP1. (*A*) Concentration-normalized scattering profiles of GPIHBP1$^{1–33}$ with Tyr^{18}–OH (2.6 mg/mL, black curve); Tyr^{18}-OSO_3 (3.8 mg/mL, blue curve); or Tyr^{18}–OPO_3 (3.6 mg/mL, green curve). (*B*) Corresponding pair–distance distribution functions [p(r)]. (*C*) Kratky plot illustrating the high flexibility and disorder of these peptides, which is best described by an ideal random-walk chain structure (58). (*D*) Heat-map representation of the flexibility in GPIHBP1$^{1–131}$ determined by HDX-MS (17), high exchange (red) to low exchange (blue). Black lines highlight sequences allowed to be flexible during EOM simulations of the SAXS data. (*E*) SEC-SAXS scattering data for a truncated GPIHBP1 lacking the acidic domain (GPIHBP1$^{34–131}$, black circles) along with the scattering profile of a rigid GPIHBP1 homology model (17) (CRYSOL; blue curve, χ^2 4.6), a model allowing glycosylation flexibility (Allosmod; red curve, χ^2 3.9), and a model allowing defined peptide flexibility (EOM; green curve, χ^2 2.4). The *Inset* shows models selected by 10 separate EOM analyses; a cartoon representation shows the nonvariable part of GPIHBP1$^{34–131}$, and dots (residues 34–42 and 74–83) or spheres (118–131) show the variable parts. The position of Trp^{89}, which is important for LPL binding, is shown in a stick representation. (*F*) SEC-SAXS scattering data for full-length GPIHBP1$^{1–131}$ with fits to a rigid homology model (CRYSOL; blue curve, χ^2 10.6) and 10 EOM analyses (green curve, χ^2 1.6). (*G*) Conformational ensembles selected for our current model of GPIHBP1$^{1–131}$ by the 10 separate EOMs. The illustration was prepared by PyMOL (Schrödinger) using the same settings as in *E* except that the spheres show residues 1–42 and dots show residues 74–83 and 118–131.

initial phase of leukocyte extravasation in the setting of inflammation. Here transient interactions between endothelial cell P-selectin and the leukocyte mucin PSGL-1 cause rolling of leukocytes along the vascular endothelium (45). Like GPIHBP1, PSGL-1 contains an N-terminal IDR that is relatively acidic with three sulfated tyrosines. Interestingly, the affinity of PSGL-1 for P-selectin increases two- to fivefold by cooperative binding via its sulfated tyrosine residues and an adjacent O-linked glycan (46, 47). This cooperativity is functionally important and translates into more efficient leukocyte rolling (45). Whether any cooperativity exists between marginated TRLs and the LPL–GPIHBP1 complex on endothelial cells, and whether GPIHBP1's IDR or its tyrosyl-O-sulfate plays a role in this process, is unclear. However, it is noteworthy that several of the apolipoproteins on the surface of TRLs have heparin-binding motifs, and it is quite conceivable that the fast binding kinetics that characterizes interactions between GPIHBP1's IDR and LPL also applies to interactions with TRL apolipoproteins. It is easy to imagine a scenario in which the formation of a ternary GPIHBP1–LPL–TRL complex constitutes the functional unit for hydrolyzing the triglycerides within TRLs. Circumstantial evidence supports this possibility (48–50).

Finally, we showed that the sulfate moiety on GPIHBP1 Tyr^{18} improves the capacity of GPIHBP1 to protect LPL against ANGPTL4-mediated unfolding, thereby improving the protection and longevity of the catalytic activity of GPIHBP1-bound LPL within capillaries. Such functional importance suggests that the sulfated tyrosine in GPIHBP1's IDR could engage LPL in a specific, albeit transient, interaction and thus act to preserve the structural integrity of LPL. Evolutionarily conserved motifs within IDRs are often functionally important (51), and the tyrosine sulfation in GPIHBP1 may represent one more example of this correlation.

Posttranslational modification with tyrosine sulfate occurs in the *trans*-Golgi network where two tyrosylprotein sulfotransferases, TPST1 and TPST2, catalyze the sulfate transfer from an activated donor. This molecule (*3′*-phosphoadenosine-*5′*-phosphosulfate) is transported to the *trans*-Golgi from the cytosol by the solute carrier family 35 member B2 (SLC35B2). It would therefore be interesting to test if loss-of-function mutations in TPST or SLC35B2 are associated with increased plasma triglyceride levels. A genome-wide CRISPER screen identified TPST2 and SLC35B2 as essential host dependency factors for the entry of HIV, and this was causally related to the tyrosine sulfation of CCR5 (52).

The current studies add substantially to our understanding of the biochemistry and physiology of intravascular triglyceride metabolism, but key mechanistic issues remain unsolved. For example, how does ANGPTL4 catalyze an ATP-independent protein unfolding regulating LPL activity? Also, how does GPIHBP1 antagonize this unfolding? The answers are unknown, but our studies would suggest that GPIHBP1's IDR and its sulfated tyrosine play central roles in this process.

Materials and Methods

Purified Proteins and Synthetic Peptides. Recombinant and secreted versions of human GPIHBP1$^{1–131/R38G}$ and murine GPIHBP1$^{1–178}$ were produced in *Drosophila* S2-cells as fusion proteins with an N-terminal human uPAR D3 tag (53) and purified as described (17). Bovine LPL (bLPL) was purified from fresh bovine milk (54). The coiled-coil domain of ANGPTL4 (residues 1–159 with an N-terminal

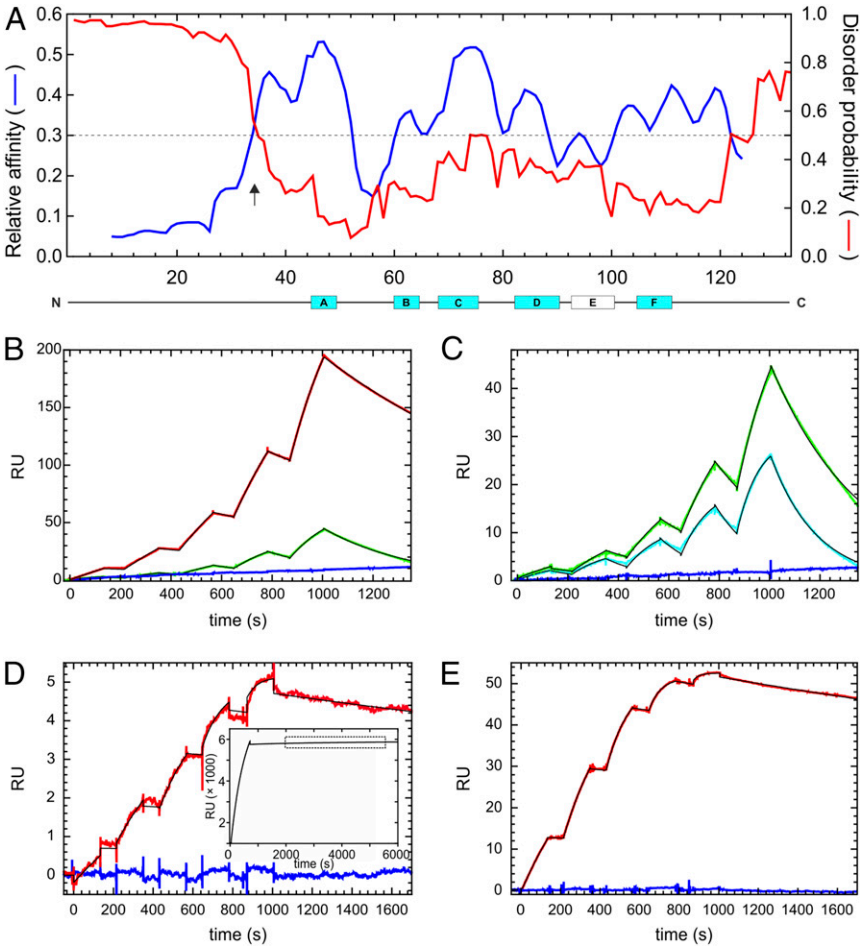

Fig. 7. Reactivity of GPIHBP1 autoantibodies purified from a subject with the GPIHBP1 autoantibody syndrome. (*A*) A comparison of the predicted IDRs and reactivity with MHC class II for GPIHBP1. Disorder prediction was assessed by IUPred (59), and reactivity with a MHC class II receptor (HLA-DRB1101 allele) was predicted by NetMHCIIpan version 3.1 (60) using a 15-mer sequence window. The cyan boxes show the positions of predicted secondary structure elements (β-strands). (*B* and *C*) Definition of the domain reactivity of a monoclonal antibody against human GPIHBP1 (mAb RF4) by single-cycle kinetics of twofold dilutions (2–32 nM) of GPIHBP1$^{1–131}$ (red curve in *B*), GPIHBP1$^{1–45}$ (green curves in *B* and *C*), GPIHBP1$^{34–131}$ (blue curve in *B*), GPIHBP1$^{27–44}$ (cyan curve in *C*), and GPIHBP1$^{27–44/R33M}$ (blue curve in *C*). (*D*) Single-cycle kinetics of 2–32 nM GPIHBP1$^{34–131}$ binding to Protein G–captured total IgG (2 μg/mL) isolated either from a patient with GPIHBP1 autoantibody syndrome [patient 102 (15), red curve] or from a healthy normolipidemic control subject (blue curve). The *Inset* shows the level of Protein G–captured immunoglobulins, and the box represents the GPIHBP1 binding segment, which is enlarged in the main figure. Comparisons of capture levels and the calculated binding capacities for GPIHBP1 reveal that 2.2 ± 0.3% (n = 9) of the total IgG fraction binds GPIHBP1$^{34–131}$. (*E*) Binding profiles for affinity-purified GPIHBP1 autoantibodies to 2–32 nM GPIHBP1$^{34–131}$ (red curve) or to GPIHBP1$^{1–45}$ (blue curve). These studies showed that 78 ± 7% (n = 4) of the affinity-purified IgG binds to GPIHBP1$^{34–131}$ (red curve), whereas none of the autoantibodies binds to GPIHBP1's acidic IDR. Thin black lines in *B*–*E* show the kinetic fit of the data to a 1:1 binding model.

methionine and a C-terminal 6× His-tag) was produced in *Escherichia coli* (55). A mouse monoclonal antibody against sulfotyrosine (mAb 1C-A2) was from Merck Millipore. Defined heparan sulfate oligomers were from Iduron and are listed in *SI Appendix*, Table S3.

Synthetic peptides representing various truncations and modifications of the N-terminal acidic domain of GPIHBP1 were obtained at a purity of >95% from TAG-Copenhagen A/S and are listed in *SI Appendix*, Table S3. Peptides with tyrosine sulfate modifications were prepared in-house by standard solid-phase peptide Fmoc synthesis with orthogonal protection of sulfotyrosine residues with a neopentyl-protected cassette [Fmoc–Tyr(OSO_3nP)–OH] as described (56). Quantitative derivatization of Tyr^{18} in GPIHBP1$^{1–33}$ with tyrosyl-O-sulfate was verified by ^{1}H-NMR (*SI Appendix*, Fig. S8). Due to the lack (or paucity) of aromatic amino acids, peptide concentrations were determined by absorbance at 214 nm using calculated molar extinction coefficients (57).

Kinetics of LPL–GPIHBP1 Binding Assessed by SPR. Reaction kinetics between LPL and GPIHBP1 derivatives were measured with a Biacore T200 instrument using a modified version of a previous protocol (17). In brief, we immobilized an anti-LPL monoclonal antibody (5D2) on a CM4 chip and then captured 150 nM bLPL in 10 mM Hepes (pH 7.4), 300 mM NaCl, 4 mM $CaCl_2$, 10% (vol/vol) glycerol, 0.05% (vol/vol) surfactant P20, 1 mg/mL defatted BSA, 0.1 mg/mL carboxylmethyl dextran, and 0.05% (wt/vol) NaN_3. This protocol kept the LPL catalytically active and led to capture densities of 150 resonance units (RUs) (approximately 3 fmol LPL/mm^2). We used single-cycle kinetics to determine the interaction between the captured LPL and the various GPIHBP1 derivatives in 10 mM Hepes (pH 7.4), 150 mM NaCl, 4 mM $CaCl_2$, 0.05% (vol/vol) P20, 0.2 mg/mL defatted BSA, and 0.05% (wt/vol) NaN_3. This protocol included five consecutive injections of twofold dilutions of GPIHBP1 (ranging from 0.125–2 nM and/or 0.25–4 nM) at a flowrate of 50 μL/min at 20 °C. At the end of each cycle, two 10-μL injections of 20-mM H_3PO_4 regenerated the chip. The recorded sensorgrams were double-buffer referenced, and the binding rate constants were calculated by fitting the data to a simple bimolecular interaction model with the mathematical model developed for single-cycle kinetics (T200 Evaluation Software 3.0; GE Healthcare).

GPIHBP1-Mediated Mobilization of LPL from a High-Density HSPG Surface. To create a surrogate high-density HSPG surface and thus mimic the conditions in the subendothelial spaces, we captured well-defined biotinylated heparin dp4 fragments (*SI Appendix*, Table S3) on a streptavidin-coupled CM5 sensor chip. The reference surface contained the nonsulfated fragment M09 S00, and the active surface contained M09 S08a with N- and O-6-sulfations (Iduron). Only the sulfated oligosaccharide bound LPL, and this yielded only weak and transient interactions. We chose to use very high surface densities (300 fmol/mm^2) of the two heparin fragments to enable the surface confinement of LPL via a dominating mass transport limitation. In each cycle, 100 nM LPL was loaded for 50 s at a flow rate of 50 μL/min in 10 mM Hepes (pH 7.4), 150 mM NaCl, 4 mM $CaCl_2$, 10% (vol/vol) glycerol, 0.05% (vol/vol) surfactant P20, 1 mg/mL defatted BSA, 1 μM GPIHBP1$^{1–33:Tyr\text{-}OH}$, and 0.05% (wt/vol) NaN_3. The synthetic GPIHBP1 peptide stabilized the LPL-loading sample during the SPR experiment, ensuring a uniform capture level. This procedure resulted in capture levels of 13 fmol/mm^2 LPL. The ability of GPIHBP1 to bind and extract LPL from this reservoir was tested by injecting 200 nM of GPIHBP1 for 1,000 s at 20 μL/min in 10 mM Hepes (pH 7.4), 150 mM NaCl, 4 mM $CaCl_2$, 10% (vol/vol) glycerol, 0.05% (vol/vol) surfactant P20, 0.2 mg/mL defatted BSA, and 0.05% (wt/vol) NaN_3. At the end of each cycle, two consecutive injections of 10 μL 1-M NaCl and 3-M guanidinium chloride regenerated the chip.

Ethical Considerations. All mouse studies were approved by University of California, Los Angeles (UCLA)'s animal research committee. Human plasma samples were received at UCLA without identifiers and were therefore deemed exempt from human use approval by UCLA.

ACKNOWLEDGMENTS. We thank Gry Rasmussen and Gitte W. Haxholm for expert technical assistance, John R. Couchman (Biotech Research and

Innovation Centre, University of Copenhagen) for critical comments, and Henrik Gårdsvoll for preparing the expression vector for GPIHBP1^{Y18F}. This work was supported by Leducq Transatlantic Network Grant 12CVD04, Lundbeck Foundation Grant R230-2016-2930, NOVO Nordisk Foundation Grant NNF17OC0026868, Swedish Research Council Grant 2015-02942, and National Heart, Lung, and Blood Institute Grants HL090553 and HL087228.

1. Brahm AJ, Hegele RA (2015) Chylomicronaemia–Current diagnosis and future therapies. *Nat Rev Endocrinol* 11:352–362.
2. Fong LG, et al. (2016) GPIHBP1 and plasma triglyceride metabolism. *Trends Endocrinol Metab* 27:455–469.
3. Olivecrona G (2016) Role of lipoprotein lipase in lipid metabolism. *Curr Opin Lipidol* 27:233–241.
4. Beigneux AP, et al. (2007) Glycosylphosphatidylinositol-anchored high-density lipoprotein-binding protein 1 plays a critical role in the lipolytic processing of chylomicrons. *Cell Metab* 5:279–291.
5. Goulbourne CN, et al. (2014) The GPIHBP1-LPL complex is responsible for the margination of triglyceride-rich lipoproteins in capillaries. *Cell Metab* 19:849–860.
6. Davies BSJ, et al. (2010) GPIHBP1 is responsible for the entry of lipoprotein lipase into capillaries. *Cell Metab* 12:42–52.
7. He C, et al. (2018) NanoSIMS analysis of intravascular lipolysis and lipid movement across capillaries and into cardiomyocytes. *Cell Metab* 27:1055–1066.e3.
8. Dijk W, et al. (2015) ANGPTL4 mediates shuttling of lipid fuel to brown adipose tissue during sustained cold exposure. *eLife* 4:e08428.
9. Gusarova V, et al. (2015) ANGPTL3 blockade with a human monoclonal antibody reduces plasma lipids in dyslipidemic mice and monkeys. *J Lipid Res* 56:1308–1317.
10. Wang Y, et al. (2013) Mice lacking ANGPTL8 (Betatrophin) manifest disrupted triglyceride metabolism without impaired glucose homeostasis. *Proc Natl Acad Sci USA* 110:16109–16114.
11. Sukonina V, Lookene A, Olivecrona T, Olivecrona G (2006) Angiopoietin-like protein 4 converts lipoprotein lipase to inactive monomers and modulates lipase activity in adipose tissue. *Proc Natl Acad Sci USA* 103:17450–17455.
12. Mysling S, et al. (2016) The angiopoietin-like protein ANGPTL4 catalyzes unfolding of the hydrolase domain in lipoprotein lipase and the endothelial membrane protein GPIHBP1 counteracts this unfolding. *eLife* 5:e20958.
13. Sonnenburg WK, et al. (2009) GPIHBP1 stabilizes lipoprotein lipase and prevents its inhibition by angiopoietin-like 3 and angiopoietin-like 4. *J Lipid Res* 50:2421–2429.
14. Allan CM, et al. (2017) Mutating a conserved cysteine in GPIHBP1 reduces amounts of GPIHBP1 in capillaries and abolishes LPL binding. *J Lipid Res* 58:1453–1461.
15. Beigneux AP, et al. (2017) Autoantibodies against GPIHBP1 as a cause of hypertriglyceridemia. *N Engl J Med* 376:1647–1658.
16. Hu X, et al. (2017) GPIHBP1 autoantibodies in a patient with unexplained chylomicronemia. *J Clin Lipidol* 11:964–971.
17. Mysling S, et al. (2016) The acidic domain of the endothelial membrane protein GPIHBP1 stabilizes lipoprotein lipase activity by preventing unfolding of its catalytic domain. *eLife* 5:e12095.
18. Babu MM (2016) The contribution of intrinsically disordered regions to protein function, cellular complexity, and human disease. *Biochem Soc Trans* 44:1185–1200.
19. Kulkarni P, et al. (2017) Phosphorylation-induced conformational dynamics in an intrinsically disordered protein and potential role in phenotypic heterogeneity. *Proc Natl Acad Sci USA* 114:E2644–E2653.
20. Bah A, et al. (2015) Folding of an intrinsically disordered protein by phosphorylation as a regulatory switch. *Nature* 519:106–109.
21. Mabashi-Asazuma H, Kuo CW, Khoo KH, Jarvis DL (2015) Modifying an insect cell N-glycan processing pathway using CRISPR-Cas technology. *ACS Chem Biol* 10: 2199–2208.
22. Gårdsvoll H, Werner F, Søndergaard L, Danø K, Ploug M (2004) Characterization of low-glycosylated forms of soluble human urokinase receptor expressed in Drosophila Schneider 2 cells after deletion of glycosylation-sites. *Protein Expr Purif* 34:284–295.
23. Kehoe JW, et al. (2006) Using phage display to select antibodies recognizing post-translational modifications independently of sequence context. *Mol Cell Proteomics* 5:2350–2363.
24. Monigatti F, Gasteiger E, Bairoch A, Jung E (2002) The sulfinator: Predicting tyrosine sulfation sites in protein sequences. *Bioinformatics* 18:769–770.
25. Pan Z, et al. (2014) Systematic analysis of the in situ crosstalk of tyrosine modifications reveals no additional natural selection on multiply modified residues. *Sci Rep* 4:7331.
26. Zhou HX, Bates PA (2013) Modeling protein association mechanisms and kinetics. *Curr Opin Struct Biol* 23:887–893.
27. Schreiber G, Haran G, Zhou HX (2009) Fundamental aspects of protein-protein association kinetics. *Chem Rev* 109:839–860.
28. Borgia A, et al. (2018) Extreme disorder in an ultrahigh-affinity protein complex. *Nature* 555:61–66.
29. Iozzo RV, Schaefer L (2015) Proteoglycan form and function: A comprehensive nomenclature of proteoglycans. *Matrix Biol* 42:11–55.
30. Dallinga MG, Dallinga-Thie GM (2016) Role of sulfatase 2 in lipoprotein metabolism and angiogenesis. *Curr Opin Lipidol* 27:181–186.
31. Ledin J, et al. (2004) Heparan sulfate structure in mice with genetically modified heparan sulfate production. *J Biol Chem* 279:42732–42741.
32. Lookene A, Chevreuil O, Ostergaard P, Olivecrona G (1996) Interaction of lipoprotein lipase with heparin fragments and with heparan sulfate: Stoichiometry, stabilization, and kinetics. *Biochemistry* 35:12155–12163.
33. Spillmann D, Lookene A, Olivecrona G (2006) Isolation and characterization of low sulfated heparan sulfate sequences with affinity for lipoprotein lipase. *J Biol Chem* 281:23405–23413.
34. Duchesne L, et al. (2012) Transport of fibroblast growth factor 2 in the pericellular matrix is controlled by the spatial distribution of its binding sites in heparan sulfate. *PLoS Biol* 10:e1001361.
35. Guttman M, Weinkam P, Sali A, Lee KK (2013) All-atom ensemble modeling to analyze small-angle X-ray scattering of glycosylated proteins. *Structure* 21:321–331.
36. Beigneux AP, et al. (2011) Assessing the role of the glycosylphosphatidylinositol-anchored high density lipoprotein-binding protein 1 (GPIHBP1) three-finger domain in binding lipoprotein lipase. *J Biol Chem* 286:19735–19743.
37. Mitić NS, Pavlović MD, Jandrlić DR (2014) Epitope distribution in ordered and disordered protein regions–Part A. T-cell epitope frequency, affinity and hydropathy. *J Immunol Methods* 406:83–103.
38. Guy AJ, et al. (2015) Insights into the immunological properties of intrinsically disordered malaria proteins using proteome scale predictions. *PLoS One* 10:e0141729.
39. Hu X, et al. (2017) Monoclonal antibodies that bind to the Ly6 domain of GPIHBP1 abolish the binding of LPL. *J Lipid Res* 58:208–215.
40. Balasubramanian R, Zhang X (2016) Mechanisms of FGF gradient formation during embryogenesis. *Semin Cell Dev Biol* 53:94–100.
41. Yan D, Lin X (2009) Shaping morphogen gradients by proteoglycans. *Cold Spring Harb Perspect Biol* 1:a002493.
42. Kleinschmit A, et al. (2010) Drosophila heparan sulfate 6-O endosulfatase regulates Wingless morphogen gradient formation. *Dev Biol* 345:204–214.
43. Merkel M, Eckel RH, Goldberg IJ (2002) Lipoprotein lipase: Genetics, lipid uptake, and regulation. *J Lipid Res* 43:1997–2006.
44. Bishop JR, et al. (2010) Deletion of the basement membrane heparan sulfate proteoglycan type XVIII collagen causes hypertriglyceridemia in mice and humans. *PLoS One* 5:e13919.
45. Zarbock A, Ley K, McEver RP, Hidalgo A (2011) Leukocyte ligands for endothelial selectins: Specialized glycoconjugates that mediate rolling and signaling under flow. *Blood* 118:6743–6751.
46. Somers WS, Tang J, Shaw GD, Camphausen RT (2000) Insights into the molecular basis of leukocyte tethering and rolling revealed by structures of P- and E-selectin bound to SLe(X) and PSGL-1. *Cell* 103:467–479.
47. Sako D, et al. (1995) A sulfated peptide segment at the amino terminus of PSGL-1 is critical for P-selectin binding. *Cell* 83:323–331.
48. Shu X, et al. (2010) Intravenous injection of apolipoprotein A-V reconstituted high-density lipoprotein decreases hypertriglyceridemia in apoav-/- mice and requires glycosylphosphatidylinositol-anchored high-density lipoprotein-binding protein 1. *Arterioscler Thromb Vasc Biol* 30:2504–2509.
49. Gin P, et al. (2008) The acidic domain of GPIHBP1 is important for the binding of lipoprotein lipase and chylomicrons. *J Biol Chem* 283:29554–29562.
50. Gin P, et al. (2011) Binding preferences for GPIHBP1, a glycosylphosphatidylinositol-anchored protein of capillary endothelial cells. *Arterioscler Thromb Vasc Biol* 31: 176–182.
51. Nguyen Ba AN, et al. (2012) Proteome-wide discovery of evolutionary conserved sequences in disordered regions. *Sci Signal* 5:rs1.
52. Park RJ, et al. (2017) A genome-wide CRISPR screen identifies a restricted set of HIV host dependency factors. *Nat Genet* 49:193–203.
53. Gårdsvoll H, Hansen LV, Jørgensen TJ, Ploug M (2007) A new tagging system for production of recombinant proteins in Drosophila S2 cells using the third domain of the urokinase receptor. *Protein Expr Purif* 52:384–394.
54. Bengtsson-Olivecrona G, Olivecrona T (1991) Phospholipase activity of milk lipoprotein lipase. *Methods Enzymol* 197:345–356.
55. Robal T, Larsson M, Martin M, Olivecrona G, Lookene A (2012) Fatty acids bind tightly to the N-terminal domain of angiopoietin-like protein 4 and modulate its interaction with lipoprotein lipase. *J Biol Chem* 287:29739–29752.
56. Stone MJ, Payne RJ (2015) Homogeneous sulfopeptides and sulfoproteins: Synthetic approaches and applications to characterize the effects of tyrosine sulfation on biochemical function. *Acc Chem Res* 48:2251–2261.
57. Kuipers BJ, Gruppen H (2007) Prediction of molar extinction coefficients of proteins and peptides using UV absorption of the constituent amino acids at 214 nm to enable quantitative reverse phase high-performance liquid chromatography-mass spectrometry analysis. *J Agric Food Chem* 55:5445–5451.
58. Kohn JE, et al. (2004) Random-coil behavior and the dimensions of chemically unfolded proteins. *Proc Natl Acad Sci USA* 101:12491–12496.
59. Dosztányi Z, Csizmok V, Tompa P, Simon I (2005) IUPred: Web server for the prediction of intrinsically unstructured regions of proteins based on estimated energy content. *Bioinformatics* 21:3433–3434.
60. Andreatta M, et al. (2015) Accurate pan-specific prediction of peptide-MHC class II binding affinity with improved binding core identification. *Immunogenetics* 67: 641–650.